Radio-frequency wave interactions with a plasma sheath in oblique-angle magnetic fields using a sheath impedance model

This manuscript was accepted by Phys. Plasmas. Click here to see the version of record.

Radio-frequency wave interactions with a plasma sheath in oblique-angle magnetic fields using a sheath impedance model

H. Kohno[1,a)] and J. R. Myra[2]

[1]*Department of Mechanical Information Science and Technology, Kyushu Institute of Technology, 680-4 Kawazu, Iizuka, Fukuoka 820-8502, Japan*

[2]*Lodestar Research Corporation, 2400 Central Avenue P-5, Boulder, CO 80301, USA*

[a)] Electronic mail: kohno@mse.kyutech.ac.jp

Abstract

The physics of interactions between waves in plasmas and sheaths for background magnetic fields which make oblique angles with the sheath surfaces is studied with the use of the self-consistent finite element code rfSOL incorporating the recently developed sheath impedance model [J. R. Myra, Phys. Plasmas **24**, 072507 (2017)]. The calculation based on this model employs the generalized sheath boundary condition (sheath BC), which surpasses the previously used capacitive sheath BC in reliability by taking into account the contributions of the ion and electron currents in the sheath as well as the displacement current. A series of numerical simulations is carried out in two-dimensional slab geometry with a flat or curved sheath surface as part of the boundary. It is shown that the sheath–plasma wave appears when the equilibrium magnetic field line angle with respect to the sheath surface is small, the absolute value of the radio-frequency (RF) sheath voltage is large, and the plasma density is slightly higher than the lower hybrid resonance density (LHR density), all of which bring the sheath property closer to being capacitive. It is also shown that the sharp variation of the magnetic field line angle along the sheath surface can sensitively affect the maximum absolute value of the RF sheath voltage at a plasma density slightly lower than the LHR

density.

PACS: 52.35.Mw, 52.40.Kh, 52.50.Qt, 52.55.Fa

I. INTRODUCTION

Waves in the ion cyclotron range of frequencies (ICRF)[1] are employed for auxiliary heating and current drive on many present day tokamaks and are expected to play an important role in future devices because of their cost effectiveness and flexibility. However, it has been known for some time[2] that ICRF waves can have strong interactions with the edge plasma and vessel surfaces. Nonlinear effects including radio-frequency (RF) sheaths and ponderomotive force have been suggested as possible mechanisms. (See Ref. 3 for a brief review.) The formation of sheaths driven by ICRF fields has received considerable attention because these sheaths can potentially create "rectified" direct-current (DC) sheath potentials[4] which accelerate ions into the surface with high energies, enhancing sputtering, and releasing impurities. Sheath potentials may also enhance transport and antenna interaction through $\mathbf{E}\times\mathbf{B}$ convection,[5–7] and RF power dissipated in the sheath may be deposited on the surfaces, leading to surface heating and possible damage. In order to alleviate these unwanted effects, several techniques to minimize RF sheath voltages have been advanced, such as choosing an optimal balance of current in the antenna straps,[8] careful field alignment of the antenna with

the magnetic field,[9] and wall boronization.[10]

In addition to the experimental effort, considerable attention has been placed on modeling RF interactions with the plasma edge.[11–19] Because of the scale separation between the Debye-scale sheath and the much larger scale length of ICRF waves, or the plasma volume, RF sheath effects have typically been described in full wave codes by using a sheath boundary condition (sheath BC). The earliest sheath models employed for this purpose described the sheath as a capacitive layer between the main plasma and the wall.[20–23] It was shown in particle-in-cell simulations that this approximation works well under conditions where the wave frequency exceeds the ion plasma frequency.[24] Recently, a generalization of the capacitive sheath BC was proposed, applicable for a wide range of RF frequencies, voltages, magnetic field line angles, and degrees of ion magnetization.[25] This generalized sheath BC was cast in terms of an effective surface impedance parameter which was calculated numerically for a large number of cases and fit to asymtotically motivated interpolation functions.[26] This constitutes a sub-grid Debye-scale model of the sheath which may be used in global RF codes. Measurements in dedicated laboratory experiments such as the Large Plasma Device (LAPD),[27] Ion cyclotron Sheath Test ARrangement (IShTAR),[28] the Prototype-Material Plasma Exposure eXperiment (Proto-MPEX),[29] and ALINE[30] are expected to provide an opportunity for validation of these models.

Various full wave RF codes have implemented some form of a sheath BC to model the interaction of RF waves with material surfaces. The "wide-sheath" limit of a capacitive sheath has been implemented in the SSWICH (self-consistent sheaths and waves for ion cyclotron heating) model[31,32] and this model, combined with RF field calculations from other codes, has been used to model sheath voltages and RF driven convection in the Tore Supra tokamak[33,34] and ASDEX Upgrade (Axially Symmetric Divertor Experiment).[35] A capacitive sheath model incorporating the Child–Langmuir law for the sheath width was implemented in the rfSOL code[36] and the properties of this system, including the sheath–plasma wave (SPW) resonance were studied.[12] The rfSOL code is a self-consistent finite element code and is aimed at solving nonlinear sheath–plasma interaction problems in the scrape-off layer (SOL) of a tokamak. More recently, the generalized RF sheath BC was implemented and tested in rfSOL[19] for the case where the background magnetic field is aligned along the normal vector to surface (the "perpendicular sheath" problem); a numerical solution obtained using this code was also compared with the one obtained by a post-processing method for a high-density plasma, and they were in good agreement with each other.[37] In addition, it was also seen in Ref. 19 that the maximum surface power density (i.e., the maximum value of P_{yz} defined later) increases almost linearly with the maximum RF sheath voltage. This is consistent with several experimental results in which the power fluxes onto ICRF antenna structures scale

linearly with the RF voltage in the transmission lines feeding the antennas.[38,39].

In the present paper, we consider the more general case where the magnetic field is at an oblique angle to the surface. The magnetic field line angle affects the wave propagation and boundary interaction as well as explicitly changing the sheath impedance. In this paper, we also compare cases where the wall is flat with cases where it has a curved surface with a scale length comparable to the tangential wavelength of the incident RF wave. In order to study basic wave and sheath interaction physics, we employ semi-infinite two-dimensional (2D) slab domains instead of realistic tokamak geometry. This simplified geometry is useful to get insight into the fundamentals of the sheath–plasma interactions which could occur on many different surfaces in a real tokamak under a variety of conditions. Examples include the protection limiters surrounding an antenna, other more distant limiters, divertor plates or associated hardware, diagnostic equipment in the SOL, and the tokamak inner wall. The local magnetic field geometry and plasma parameters differ in each case.

The paper is organized as follows. In Sec. II, we describe the equations used for solving macroscopic sheath–plasma interaction problems and briefly summarize the main feature of the new rfSOL code. In Sec. III, numerical results obtained from calculations in 2D slab domains with a flat sheath surface are presented together with some analytical investigations; here, the differences between the results obtained under the capacitive and

generalized sheath BCs are discussed. The effect of the wall shape on various quantities on the sheath surface at relatively low plasma densities is analyzed in Sec. IV. Finally, a summary and conclusions of the present work are given in Sec. V.

II. FORMULATION FOR RF SHEATH–PLASMA INTERACTIONS

In this section, we summarize the equations that describe macroscopic interactions between waves in plasmas and sheaths on metal surfaces. In the following analysis, we assume that only deuterium is considered as an ion species.

The governing equation for waves in plasmas is a combined form of Maxwell's equations described as

$$\nabla\times\nabla\times\mathbf{E}-\frac{\omega^2}{c^2}\boldsymbol{\varepsilon}\cdot\mathrm{E}-\mathrm{i}\omega\mu_0\mathbf{J}_{\mathrm{ext}}=\mathbf{0}, \tag{1}$$

where the electric field $\mathbf{E}$ and the external current density $\mathbf{J}_{\mathrm{ext}}$ vary on the RF time scale. Here, i is the imaginary unit, ω is the applied angular frequency, c is the speed of light, having a relation with the dielectric constant ε_0 and the permeability μ_0 in vacuum. The dielectric tensor $\boldsymbol{\varepsilon}$ is given based on the cold plasma model.[1] Throughout this study, we assume that quasi-neutrality is retained in the plasma region, i.e., $n_{\mathrm{e0}} = n_{\mathrm{i0}} = n_0$, where n_{e0} and n_{i0} are the equilibrium number densities of electrons and ions, respectively.

This manuscript was accepted by Phys. Plasmas. Click here to see the version of record.

Hereafter, n_0 is simply called the plasma density.

The RF wave interaction with a plasma sheath on the metal wall is taken into account by means of a sheath BC,[25,26] which is written as follows:

$$\mathbf{E}_t = -\nabla_t V_{RF}. \tag{2}$$

Here, the subscript t denotes the component tangential to the sheath–plasma interface (i.e., the hypothetical boundary surface between the magnetic presheath and the plasma), and V_{RF} is the instantaneous RF voltage across the sheath, which is simply called the RF sheath voltage hereafter. With the use of the sheath impedance parameter z_{sh}, the expression for V_{RF} is

$$V_{RF} = -J_n z_{sh} = -\frac{\omega}{i} D_n z_{sh}, \tag{3}$$

where J_n ($= \mathbf{s}\cdot\mathbf{J}$) is the component of the total current density $\mathbf{J}$ normal to the sheath surface, and D_n ($= \varepsilon_0 \mathbf{s}\cdot\boldsymbol{\varepsilon}\cdot\mathbf{E}$) is the component of the electric displacement $\mathbf{D}$ normal to the sheath surface (and $\mathbf{s}$ in the definitions is the unit normal vector pointing into the plasma). Note that both J_n and D_n are quantities on the plasma side of the sheath–plasma interface. When the local magnetic field line and the sheath surface intersect at an oblique angle, the sheath impedance parameter z_{sh} is described as a function of the following four dimensionless parameters, which are evaluated on the sheath surface: $\hat{\Omega}_i = \Omega_i/\omega_{pi}$, $|b_n|$ (where $b_n = \mathbf{b}\cdot\mathbf{s}$), $\hat{\omega} = \omega/\omega_{pi}$, and $\tilde{V}_{RF} = e|V_{RF}|/T_e$, where Ω_i is the ion cyclotron frequency, ω_{pi} is the ion plasma frequency, $\mathbf{b}$ is the unit vector along the background

This manuscript was accepted by Phys. Plasmas. Click here to see the version of record.

magnetic field $\mathbf{B}_0$ (i.e., $\mathbf{b} = \mathbf{B}_0/|\mathbf{B}_0|$), e is the elementary charge, and T_e is the electron temperature. Here, $|b_n|$ can also be expressed as $|b_n| = \sin\theta$, where θ is the angle between the equilibrium magnetic field line and the metal wall (or the sheath surface); for brevity, we refer to this as the magnetic field line angle hereafter, and the "oblique-angle magnetic field" corresponds to the case where $0 < \theta < \pi/2$. To compute z_{sh}, we employ the dimensionless ion, electron, and displacement (current) admittance parameters derived in Ref. 26. These modified expressions for the ion, electron, and displacement current contributions yield almost the same (total) sheath admittance parameter as that calculated by the previous expressions[19,25] within the limits of validity of the latter, i.e., when the background magnetic field is perpendicular to the sheath surface and the dimensionless parameters $\hat{\omega}$ and $\tilde{V}_{RF}$ do not exceed the previously set upper limits, see Appendix A.

The wave propagation model for the dielectric tensor $\boldsymbol{\varepsilon}$ in the rfSOL code is the cold fluid model,[1] which is valid in the SOL but not in the core. In order to exclude the core plasma region from the calculation domain (i.e., the SOL region), when necessary, we introduce a damping layer in the vicinity of the hypothetical core–edge plasma boundary together with the conducting-wall boundary condition (conducting-wall BC) on that boundary. This is called the absorbing boundary condition (absorbing BC), and the details of this approach are described in our previous papers.[12,36] Note that in this study there is no need to

set the damping layer when the waves in the plasma do not reach the core–edge plasma boundary due to evanescence.

The combined form of Maxwell's equations and the nonlinear sheath BC are self-consistently solved using the upgraded rfSOL code, into which all the functions necessary to compute the sheath impedance parameter z_{sh} for oblique-angle magnetic fields are introduced. The present model assumes a Fourier mode in the z direction in space, and so the governing equations are numerically solved in the three-dimensional space. The calculations are performed on the Edison (Cray XC30) computer system at the National Energy Research Scientific Computing Center (NERSC).

III. SHEATH–PLASMA INTERACTIONS ON A FLAT CONDUCTING SURFACE

As the first numerical analysis, we consider sheath–plasma interaction problems in 2D slab geometry with a flat conducting surface, which were analyzed using the capacitive sheath BC in our earlier work.[12] Figure 1 shows the problem definition; here, a combined form of Maxwell's equations is solved subject to the generalized sheath BC (or the capacitive sheath BC for the purpose of comparison) on the right boundary, the absorbing BC on the left boundary (or the conducting-wall BC in the case where waves do not propagate to the left

boundary), and a periodic boundary condition (periodic BC) that connects the top and bottom of the domain. The antenna current density is given by employing a cosine function in the y direction in the range $\left(L_y - L_{\text{ant}}\right)/2 \le y \le \left(L_y + L_{\text{ant}}\right)/2$ as follows:

$$\mathbf{J}_{\text{ext}} = K(y)\delta\left(x - D_{\text{bl-ant}}\right)\mathrm{e}^{\mathrm{i}(k_z z - \omega t)}\mathbf{e}_y, \tag{4}$$

where

$$K(y) = K_{\max}\cos^2\left[\frac{\pi}{L_{\text{ant}}}\left(y - \frac{L_y}{2}\right)\right]. \tag{5}$$

Here, k_z is the z component of the wave vector $\mathbf{k}$, and $\mathbf{e}_y$ is the unit vector in the y direction. (Hereafter, the subscripts x, y, and z denote the x, y, and z components of vector quantities, respectively.) The following parameters are fixed throughout the analysis in this section: L_{ant} = 0.05 m (antenna length), C_{sh} = 0.6 used in the capacitive sheath BC,[36] T_{e} = 10 eV, k_z = 10.8 m^{-1}, and $f = \omega/2\pi$ = 80 MHz. The other parameters are determined separately in each problem considered below. The calculation domain is divided by non-uniform meshes which consist of nine-node rectangular elements. In these meshes, the nodal positions in the x direction are concentrated in the vicinity of the antenna, sheath surface, and left boundary in order to accurately resolve possible thin layers, within which waves from the antenna and/or SPWs exponentially decay; on the other hand, the nodes are uniformly distributed in the y direction. This applies to all the meshes used in this study. The numerical results shown in this and next sections are assumed to be on the plane of z =

This manuscript was accepted by Phys. Plasmas. Click here to see the version of record.

0 m at $t = 2\pi l/\omega$, where l is an integer.

A. Effect of the sheath resistance

We first investigate how the behavior of the SPW observed under the capacitive sheath BC varies when the boundary condition is replaced with the generalized sheath BC. Based on Fig. 1, the calculation domain and the antenna position are determined such that $L_x = 0.6$ m, $L_y = 0.4$ m, and $D_{\text{bl-ant}} = 0.57$ m. The maximum surface current density of the antenna, $K_{\max}$, is fixed at 1 A/m. The uniform plasma density and the background magnetic field are $n_0 = 2\times10^{18}$ m^{-3}, $B_{0x} = 1.5$ T, $B_{0y} = 0.5$ T, and $B_{0z} = 4$ T. For these parameters, both the fast and slow waves do not propagate in the cold plasma according to the local dispersion relation.[1] Thus, there is no need to form an absorbing layer on the left-hand side of the domain. The non-uniform mesh used here consists of 360 (in the x direction) × 540 (in the y direction) nine-node elements (or 721×1081 nodes) in total; 300×540 and 60×540 elements are allocated in $0 \le x \le D_{\text{bl-ant}}$ and $D_{\text{bl-ant}} \le x \le L_x$, respectively.

Figure 2(a) and (b) show the filled contour plots of the real part of the electric field component parallel to $\mathbf{B}_0$ (i.e., $E_{\parallel} = \mathbf{E}\cdot\mathbf{b}$), which are obtained by imposing the capacitive and generalized sheath BCs on the right boundary, respectively. Here, a black line segment in the plots indicates the antenna, and the black oblique lines indicate the sections of the

magnetic surfaces on the $x-y$ plane. Note that the full domain of the simulation extends back to x = 0 m and is not illustrated in Fig. 2 (or Fig. 4 shown subsequently). The large domain insures that the left-going wave is fully evanescent or absorbed without any reflection from the left boundary.

The plot shown in Fig. 2(a) is almost identical with that shown in Fig. 3(b) of Ref. 12; however, the present result is obtained using the more accurate nonlinear scheme (see Appendix A of Ref. 41) with a different grid resolution. In Fig. 2(a), we see a localized propagating wave mode along the sheath surface, i.e., a propagating SPW. This phenomenon is important because the local sheath voltage due to the presence of the SPW can be very high at higher antenna current densities, and consequently enhanced impurity sputtering may occur over a wide range of material surfaces. However, we note that this result is obtained under no sheath power dissipation based on the assumption that the sheath impedance is dominated by its capacitance. (Although the capacitive sheath impedance model *neglects* the electron particle current in the sheath relative to the displacement current, the former is not really zero as discussed next and it does give rise to power dissipation. For a discussion of power balance in a sheath and its relationship to rectification and ion impact energy, the reader is referred to Sec. IV D in Ref. 25 and a reference therein [Ref. 42; see the Appendix].)

On the other hand, as shown in Fig. 2(b), the SPW disappears when the generalized

This manuscript was accepted by Phys. Plasmas. Click here to see the version of record.

sheath BC is imposed on the right boundary even though the same parameters as in the capacitive sheath case are used.

To investigate the cause of the large difference in the above-mentioned results, we compare the values of the dimensionless sheath admittance parameter $\hat{y}_{\mathrm{sh}}$ calculated based on the two different sheath models. For the capacitive sheath model, the sheath admittance parameter is given by

$$\hat{y}_{\mathrm{sh}} = \hat{z}_{\mathrm{sh}}^{-1} = -\mathrm{i}\frac{\omega\lambda_{\mathrm{De}}}{\Delta_{\mathrm{sh}}\omega_{\mathrm{pi}}}, \tag{6}$$

where $\hat{z}_{\mathrm{sh}}$ is the dimensionless sheath impedance parameter, λ_{De} is the electron Debye length, and Δ_{sh} is the time-averaged non-neutral sheath width.[19] When the RF contribution can be neglected (as in the case here since the RF wave amplitudes are small), the sheath width is approximately expressed by[12]

$$\Delta_{\mathrm{sh}} \approx C_{\mathrm{th}}\lambda_{\mathrm{De}}, \tag{7}$$

where

$$C_{\mathrm{th}} = \left\{\ln\left[\left(\frac{m_{\mathrm{i}}}{m_{\mathrm{e}}}\right)^{1/2}|b_{\mathrm{n}}|\right]\right\}^{3/4}. \tag{8}$$

Here, m_{i} and m_{e} are the ion (deuterium) mass and the electron mass, respectively. Since only the displacement current contribution is taken into account in the capacitive sheath model, $\hat{y}_{\mathrm{sh}}$ is equivalent to the dimensionless displacement admittance parameter $\hat{y}_{\mathrm{d}}$ (i.e., the dimensionless admittance parameter for the displacement current) in this case. For the

This manuscript was accepted by Phys. Plasmas. Click here to see the version of record.

parameters used here, we obtain $\hat{y}_{sh} \approx -0.165\mathrm{i}$. Note that $\hat{y}_{sh}$ is almost constant along the sheath surface because of the very small antenna current density (recall that $K_{max} = 1$ A/m). On the other hand, the value of $\hat{y}_{sh}$ is $0.464 - 0.118\mathrm{i}$ for the generalized sheath impedance model. The breakdown of this value is as follows: $\hat{y}_i \approx 5.93\times10^{-2} - 1.67\times10^{-2}\mathrm{i}$, $\hat{y}_e \approx 0.405$, and $\hat{y}_d \approx -0.101\mathrm{i}$. (Note that $\hat{y}_{sh} = \hat{y}_i + \hat{y}_e + \hat{y}_d$, where $\hat{y}_i$ and $\hat{y}_e$ are the dimensionless ion and electron admittance parameters, respectively.[25]) We find that the ion current contribution is less important, the displacement current contribution is similar to that for the capacitive sheath model, and most importantly, the electron current contribution (which is not considered in the capacitive sheath model) is dominant. In fact, the expression for $\hat{y}_e$ is given by $\hat{y}_e = h_0|b_n|$ in the limit $\tilde{V}_{RF} \ll 1$, where $h_0 = 1.161585$;[26] therefore, the value of $\hat{y}_e$ does not approach zero in the generalized sheath BC unless the direction of $\mathbf{B}_0$ is nearly parallel to the sheath surface. Since the electron current yields a resistive effect in the sheath, this should be associated with the fact that a propagating wave mode such as the one in Fig. 2(a) is not observed under the generalized sheath BC as shown in Fig. 2(b).

The behavior of the SPW can be directly understood by applying the theory of an electrostatic 2D sheath mode to our slab model in the same way as we did using the capacitive sheath BC.[12] Here, we consider (local) sheath–plasma interactions on the sheath surface perpendicular to the x-axis; again, we assume that the plasma density and the background

This manuscript was accepted by Phys. Plasmas. Click here to see the version of record.

magnetic field are spatially uniform in the cold plasma. The presence of wave patterns near the sheath surface invokes the mode $\sim e^{i\mathbf{k}\cdot\mathbf{x}}$, where $\mathbf{x}$ is the position vector. Since we assume that the electrostatic model is valid (i.e., $\mathbf{E} = -\nabla\Phi = -i\mathbf{k}\Phi$) and $\mathbf{s} = -\mathbf{e}_x$ in this analysis, the generalized sheath BC given in Eqs. (2) and (3) is rewritten as

$$1 = -\varepsilon_0 \omega z_{sh} \mathbf{e}_x \cdot \boldsymbol{\varepsilon} \cdot \mathbf{k}. \tag{9}$$

The components of the wave vector $\mathbf{k}$ must also satisfy the electrostatic dispersion relation in the plasma, which is given by

$$\mathbf{k} \cdot \boldsymbol{\varepsilon} \cdot \mathbf{k} = 0. \tag{10}$$

Consequently, one can solve Eqs. (9) and (10) to find k_x and k_y for given ω and k_z. The Newton–Raphson method can be employed for this calculation.

Figure 3 shows the variations of the real and imaginary parts of k_y at the sheath surface as functions of the plasma density n_0 with a semi-logarithmic scale for the horizontal axis; the plot shown in Fig. 3(a) is obtained by imposing $\hat{y}_{sh} = \hat{y}_d$ on the computation of z_{sh} in Eq. (9), while the full expression for $\hat{y}_{sh}$ (i.e., $\hat{y}_{sh} = \hat{y}_i + \hat{y}_e + \hat{y}_d$) is used to obtain the plot shown in Fig. 3(b). Here, the fixed parameters are the same as those used to obtain the results in Fig. 2. Also, for the purpose of comparison with the numerical results with $K_{max} = 1$ A/m, the RF contribution to the sheath is omitted in both cases; i.e., $\tilde{V}_{RF} = 0$ in computing $\hat{z}_{sh}$. Note that the expression for $\hat{y}_d$ in the sheath impedance model[26] is different from that

given in Eqs. (6)–(8); nevertheless, the plot shown in Fig. 3(a) is very similar to the one obtained in our previous work.[12] It is seen in Fig. 3(a) and (b) that $|k_y|$ rapidly increases to infinity near the plasma density corresponding to the lower hybrid resonance (i.e., at $\varepsilon_\perp = 0$). Hereafter, this particular plasma density is called the lower hybrid resonance density (denoted by n_{LH}), which is further abbreviated to the LHR density. In contrast with the case where the capacitive sheath BC is effectively employed, the calculated values of $|\mathrm{Im}(k_y)|$ are greater than those of $|\mathrm{Re}(k_y)|$ even for $n_0 > n_{\mathrm{LH}}$ when the generalized sheath BC is employed. This indicates that there is almost no density region where the SPW appears as a propagating wave along the sheath surface under the generalized sheath BC for the parameters used in this analysis. Of course, the numerical results for the sheath impedance model are more reliable from a physical point of view, since the ion and electron current contributions (in addition to the displacement current contribution) are appropriately introduced in the generalized sheath BC.

B. SPW under the generalized sheath BC

In Sec. III A, we have confirmed that the electron current contribution in the sheath prevents the SPW from propagating along the sheath surface for a particular set of parameters if K_{max} is very small (i.e., for a thermal sheath). A qualitatively similar result was also

This manuscript was accepted by Phys. Plasmas. Click here to see the version of record.

obtained in our previous work, see Sec. 5.3 of Ref. 19. Then, the important question is whether the SPW can still be observed even under the generalized sheath BC when we employ different parameters. To demonstrate that the SPW can appear under the generalized sheath BC, we first show an illustrative example using the parameters described below.

In this numerical analysis, the components of $\mathbf{B}_0$ are specified as follows: B_{0x} = 0.5 T, B_{0y} = 1.5 T, and B_{0z} = 4 T. Thus, the magnetic field line angle θ at the sheath–plasma interface is smaller than that given in Sec. III A. Accordingly, the calculation domain and the antenna position are determined such that L_x = 0.5 m, L_y = 0.4 m, and $D_{\text{bl-ant}}$ = 0.47 m. The non-uniform mesh for the entire domain consists of 360×540 nine-node elements in total; 280×540 and 80×540 elements are allocated in $0 \le x \le D_{\text{bl-ant}}$ and $D_{\text{bl-ant}} \le x \le L_x$, respectively. The plasma density n_0 is fixed at 6×10^{17} m^{-3} (still greater than the LHR density); again, the absorbing layer need not be present on the left-hand side of the domain, since the wave is evanescent in the plasma.

Figure 4(a) and (b) show the filled contour plots of $\mathrm{Re}\left(E_{\parallel}\right)/K_{\max}$ at $K_{\max}$ = 1 A/m and $K_{\max}$ = 100 A/m, respectively, which are obtained by imposing the generalized sheath BC on the right boundary. From this figure, we see that the SPW does appear when $K_{\max}$ is increased to 100 A/m although it is not observed at $K_{\max}$ = 1 A/m.

The behavior of the SPW for the parameters given here can also be investigated using

the analytical approach described in Sec. III A. Figure 5 shows the variations of the real and imaginary parts of k_y at the sheath surface as functions of the normalized absolute value of the RF sheath voltage, $\tilde{V}_{\mathrm{RF}}$. It is seen that while $\left|\mathrm{Re}\left(k_y\right)\right| < \left|\mathrm{Im}\left(k_y\right)\right|$ for $\tilde{V}_{\mathrm{RF}} \approx 0$, this magnitude relation in one root at a large value of $\tilde{V}_{\mathrm{RF}}$ changes to $\left|\mathrm{Re}\left(k_y\right)\right| > \left|\mathrm{Im}\left(k_y\right)\right|$ with $\left|\mathrm{Im}\left(k_y\right)\right|$ being sufficiently small. This indicates that the SPW can appear only in the region where the absolute value of the RF sheath voltage is large and/or the electron temperature is low in a relatively low-density plasma. The maximum value of $|V_{\mathrm{RF}}|$ in the numerical solution for K_{max} = 100 A/m is 284 V, which corresponds to $\tilde{V}_{\mathrm{RF}}$ = 28.4. This value is indicated with a gray vertical line in Fig. 5 and gives a root of $\mathrm{Re}\left(k_y\right)$ = –58 m^{-1} and $\mathrm{Im}\left(k_y\right)$ = –11 m^{-1}. The wavelength of this SPW is then given by $\lambda_{\mathrm{SPW}} = 2\pi/58 \approx 0.11$ m, which is close to the one observed in Fig. 4(b). On the other hand, the maximum value of the surface power density P_{yz} (defined in Sec. III C) for K_{max} = 100 A/m is 81.6 kW/m^2, which is too small to cause material damage in general. Thus, the main concern would be the high sheath voltage and associated sputtering.

Although the existence of the sheath resistance makes the SPW evanescent and thus it is less critical as compared with a propagating case predicted by the capacitive sheath model (see Fig. 2(a)), the observed SPW still extends the high sheath voltage region on the material surface from where the plasma wave has interacted with the sheath. In general, we expect that

sheath resistivity should reduce the sheath voltage, but also should reduce the surface area on which the RF power deposition from the SPW occurs. The latter effect tends to increase the surface power density. The competition of these effects requires quantitative evaluation for a given case.

In order to excite the SPW, several non-negligible components in the antenna spectrum in terms of k_y need to overlap with the characteristic components in the spectrum of the SPW. Due to the finite length of the antenna and the form of the imposed antenna current, its spectrum has significant components at many values of k_y other than the dominant value, i.e., $k_{y,\mathrm{ant}} = \pi/L_{\mathrm{ant}}$. If the SPW resonance is sharp, it can be excited by even a small overlap of $k_{y,\mathrm{SPW}}$ (k_y for the SPW) with the antenna spectrum.

The appearance of the SPW is also related to the magnitude relation of the real and imaginary parts of the dimensionless sheath admittance parameter $\hat{y}_{\mathrm{sh}}$. In Sec. III A, we have seen a propagating SPW only under the capacitive sheath BC in which the sheath resistance is not included. The capacitive limit in the generalized sheath BC corresponds to the case where $\hat{y}_{\mathrm{sh}} \approx \hat{y}_{\mathrm{d}}$ with $\left|\mathrm{Re}(\hat{y}_{\mathrm{sh}})\right|$ being sufficiently small as compared with $\left|\mathrm{Im}(\hat{y}_{\mathrm{sh}})\right|$. Figure 6(a), (b), and (c) show the variations of the real and imaginary parts of $\hat{y}_{\mathrm{sh}}$ and the imaginary part of $\hat{y}_{\mathrm{d}}$ as functions of $\tilde{V}_{\mathrm{RF}}$, $|b_{\mathrm{n}}|$, and n_0, respectively. The fixed parameters necessary to compute $\hat{y}_{\mathrm{sh}}$ and $\hat{y}_{\mathrm{d}}$ in each plot are the same as those used to obtain the numerical result

This manuscript was accepted by Phys. Plasmas. Click here to see the version of record.

shown in Fig. 4(b) (although T_e and k_z are not used here); the value of $\tilde{V}_{RF}$ is fixed at 28.4 in Fig. 6(b) and (c). It can be seen that the sheath approaches the capacitive limit when the dimensionless absolute value of the RF sheath voltage is large, the magnetic field line angle is small to the extent that the sheath is regarded as the ion-rich sheath, and the plasma density is low. Note, however, that the SPW does not always appear in the capacitive limit, as demonstrated by the example in Sec. III C below.

C. Almost capacitive sheath case

As a last numerical example in this section, we consider the case where the RF sheath is formed through interaction with a propagating slow wave (SW) in a low-density plasma. Here, the RF electric field strength is varied with different values of K_{max}. The parameters used in this analysis are the same as those used in Sec. IV C of Ref. 12 (except the mesh resolution) and are described as follows: $L_x = 0.7$ m, $L_y = 0.3$ m, $D_{\text{bl-ant}} = 0.65$ m, $B_{0x} = 1.5$ T, $B_{0y} = 0.5$ T, $B_{0z} = 4$ T, $n_0 = 1\times10^{17}$ m^{-3}, $\nu_0 = 3\times10^{11}$ s^{-1}, and $\lambda_\nu = 0.05$ m, where the collision frequency for the absorbing layer is given by $\nu = \nu_0 e^{-x/\lambda_\nu}$, see Refs. 12 and 36. The non-uniform mesh for the entire domain consists of 480×460 nine-node elements in total; 420×460 and 60×460 elements are allocated in $0 \le x \le D_{\text{bl-ant}}$ and $D_{\text{bl-ant}} \le x \le L_x$, respectively.

This manuscript was accepted by Phys. Plasmas. Click here to see the version of record.

Figure 7(a) and (b) show the filled contour plots of $\mathrm{Re}\left(E_{\|}\right)/K_{\max}$ at $K_{\max}$ = 160 A/m, which are obtained by imposing the capacitive and generalized sheath BCs on the right boundary, respectively. The plot shown in Fig. 7(a), which is obtained using the improved code for the capacitive sheath model (see Sec. III A), is almost identical with that shown in Fig. 6(b) of Ref. 12. It is seen that these nonlinear results for this high antenna current density are very similar to each other, which indicates that the sheath impedance model approaches the capacitive sheath model for the given parameters. The reason for this close similarity is understood by noting that $\mathrm{Im}\left(z_{\mathrm{sh}}\right)$ is much greater than $\mathrm{Re}\left(z_{\mathrm{sh}}\right)$ in the range of the interaction with the SW, as shown in Fig. 8, which means that the effect of the sheath resistance is almost negligible.

Figure 9(a), (b), and (c) show the plots of $\left|V_{\mathrm{RF}}\right|$, V_{rect}, and P_{yz} along the sheath surface for $K_{\max}$ = 20, 40, 80, and 160 A/m under the generalized sheath BC, respectively. Here, V_{rect} is the rectified sheath voltage, which is a function of $\hat{\omega}$ and $\tilde{V}_{\mathrm{RF}}$.[26] (Note that the total sheath voltage V_{total} is given by $V_{\mathrm{total}} = V_{\mathrm{RF}} + V_{\mathrm{rect}}$, and the thermal contribution in V_{rect} is $C_{\mathrm{th}}^{4/3} T_{\mathrm{e}}/e \approx 30$ V.[12]) The quantity P_{yz} is defined on the sheath surface (i.e., on the $y-z$ plane at $x = L_x$) as[19]

$$P_{yz} \equiv \frac{1}{2}\left|J_x\right|^2 \mathrm{Re}\left(z_{\mathrm{sh}}\right) = \frac{1}{2}\left|V_{\mathrm{RF}}\right|^2 \mathrm{Re}\left(y_{\mathrm{sh}}\right) = \frac{1}{2}\left|V_{\mathrm{RF}}\right|^2 \sum_{j=\mathrm{i,e}} \mathrm{Re}\left(y_j\right), \tag{11}$$

where y_{i} and y_{e} are the ion and electron admittance parameters, respectively; note that the

displacement current contribution is not associated with any power loss. Physically, in the microscopic description, P_{yz} arises from RF power dissipation in the volume of the sheaths; however, as discussed in Appendix C of Ref. 19, from the macroscopic point of view this may be interpreted as a locally dissipated power per unit area on the sheath surface. (The admittance form of P_{yz} is provided here for completeness and may be used to evaluate the power loss in the electron and ion channels at the sheath surface, i.e., *at the magnetic presheath entrance*. See Sec. IV D of Ref. 25 for a discussion of the power split at the actual wall. Note also that here we evaluate only the power impacting the surface that arises from the RF electrodynamic interaction with the sheath, specifically from $\mathbf{J}_{\mathrm{RF}} \cdot \mathbf{E}_{\mathrm{RF}}$. DC contributions to the surface heat load, such as from thermal contributions, are not included.) Hereafter, P_{yz} is simply called the surface power density (defined on the $y-z$ plane).

It is seen in Fig. 9(a) and (b) that the maximum values of $|V_{\mathrm{RF}}|$ and V_{rect} rapidly increase with the increase in $K_{\max}$ and reach the order of a few kilovolts at $K_{\max}$ = 160 A/m. Such high voltages will greatly enhance the impurity sputtering yield on a metal wall; the low plasma density considered in this example will reduce the number of *directly* sputtered impurities, but self-sputtering avalanches may still be a concern. The maximum values of V_{rect} are smaller than those of $|V_{\mathrm{RF}}|$ at the same values of $K_{\max}$ and are similar to those of V_0 (the rectified sheath potential based on the Child–Langmuir law) shown in Fig. 8 of Ref.

12. Hereafter, we will show $|V_{RF}|$ as a measure of the sheath voltage that is relevant to ion acceleration and sputtering. For high-frequency RF sheaths, $\omega >> \omega_{pi}$, the rectified sheath voltage, which is directly related to $|V_{RF}|$ (see Fig. 6 of Ref. 25), provides the actual voltage through which the ions are accelerated; in the opposite limit, $\omega << \omega_{pi}$, the instantaneous value of V_{total} (bounded by $V_{rect} \pm |V_{RF}|$) provides a more useful measure of ion acceleration.

On the other hand, as shown in Fig. 9(c), the maximum surface power density for K_{max} = 160 A/m is approximately 360 kW/m^2, at which value serious material damage may not occur. Low surface power densities at a low-density plasma were also seen in our previous work; see Fig. 8 of Ref. 19. For comparison, in the sheath-limited (collisionless) regime, the heat flux for a thermal plasma without RF is estimated as $S_E n_0 T_e c_s$, where S_E is the sheath energy transmission coefficient and $c_s = (T_e/m_i)^{1/2}$.[43] For $T_e = T_i$ we find that $S_E \sim 7.3$, and the DC reference heat flux for the parameters in this analysis is 26 kW/m^2. This is still small compared with the RF contribution.

IV. SHEATH–PLASMA INTERACTIONS ON A SHAPED WALL

As the second numerical analysis, we consider the interactions between SWs and sheaths in 2D slab geometry with a shaped wall in the form of a conducting bump. The

This manuscript was accepted by Phys. Plasmas. Click here to see the version of record.

purpose of this section is to investigate the effect of the variation in $|b_n|$ (or the magnetic field line angle) on the quantities related to sheaths based on the fact that plasmas are in contact with various shapes of material surfaces in the SOL of tokamaks. The geometrical configuration of the simulation is the same as that used in Sec. III (i.e., Fig. 1) except that a Gaussian-shaped bump is located on the right boundary (see Fig. 10); here, the generalized sheath BC is imposed on the sheath surface including the slopes of the bump. The local height of the bump, h_{sh}, is given by

$$h_{sh}(y) = h_{bump} \exp\left[-\frac{(y - L_y/2)^2}{w_{bump}^2}\right]. \quad (12)$$

The following parameters are fixed throughout the analysis in this section: L_x = 6 m, L_y = 0.8 m, $D_{bl\text{-}ant}$ = 5.2 m, L_{ant} = 0.4 m, w_{bump} = 0.1 m, T_e = 15 eV, k_z = 160 m^{-1}, f = 80 MHz, ν_0 = 3×10^{11} s^{-1}, and λ_ν = 0.4 m. The non-uniform mesh for the entire domain consists of 800×200 nine-node elements in total; 600×200 and 200×200 elements are allocated in $0 \le x \le D_{bl\text{-}ant}$ and $D_{bl\text{-}ant} \le x \le L_x - h_{sh}$, respectively. In this numerical analysis, we examine two cases using two different values of the plasma density n_0 with the background magnetic field $\mathbf{B}_0$ oriented purely or mostly in the x direction.

A. Lower density case

First, we consider the case where n_0 = 1×10^{17} m^{-3}, B_{0x} = 4 T, B_{0y} = 0 T, and B_{0z}

= 0 T in the entire slab domain. Here, K_{max} is fixed at 600 A/m, while the maximum height of the bump, h_{bump}, is varied in the range of 0 to 0.4 m; of course, h_{bump} = 0 m corresponds to the flat sheath surface (i.e., no bump). The distance between the antenna and the sheath surface varies according to the height of the bump when the antenna position is kept fixed. However, it should be kept in mind that, according to the super-position principle, the left-going waves reflected off the right boundary (or the bump) pass through the antenna as if it were not there, since the antenna current is given solely as a source for generating the RF field in the present study (see Eqs. (1) and (4)). Therefore, moving the antenna (or varying $D_{bl\text{-}ant}$ in Fig. 10) only changes the phase of the electric field on the surface of the bump; i.e., it does not change the spatial variations of the absolute values of the quantities, e.g., $|V_{RF}|$, $|z_{sh}|$, $|E_{\|}|$, and $|D_n|$ on the sheath surface from which the propagating waves are reflected (see Fig. 12 later).

Figure 11 shows the filled contour plot of $\mathrm{Re}(E_{\|})/K_{max}$ at h_{bump} = 0.4 m, which illustrates the interaction of the propagating SW with a bump. We see that the electric field strength near the steepest angles of the bump (i.e., near the minimum value of $|b_n|$) is sufficiently close to the maximum of the propagating wave fronts for the given parameters. The spatial variations of $|V_{RF}|$, $|z_{sh}|$, $|E_{\|}|$, and $|D_n|$ on the sheath surface at four different values of h_{bump} are shown in Fig. 12. Note that these variations are given as functions of y

This manuscript was accepted by Phys. Plasmas. Click here to see the version of record.

instead of τ, which increases along the sheath surface (see Fig. 10). From this figure, we find that $|V_{RF}|$ and $|D_n|$ decrease with the bump height, $|z_{sh}|$ is nearly independent of the bump height, and $|E_{||}|$ increases strongly with the bump height. Although not shown here, the spatial variations of P_{yz} are qualitatively similar to those of $|V_{RF}|$, and the maximum value of P_{yz} is approximately 70 kW/m^2 at h_{bump} = 0 m; by the presence of the bump, the calculation method for the surface power density P_{yz} needs to be generalized as $P_{yz} = P_{\tau z}(\mathrm{d}\tau/\mathrm{d}y) = P_{\tau z}/|b_n|$, where $P_{\tau z}$ (= $|J_n|^2 \mathrm{Re}(z_{sh})/2$) is the local surface power density on the $\tau - z$ plane parallel to the sheath surface.

The minimum value of $|b_n|$, at which the strongest interactions occur, varies by a factor of 3.6 in the range of h_{bump} = 0 to 0.4 m. Thus, on the slopes of the bump, the rate of decrease in $|b_n|$ with h_{bump} is greater than the rate of increase in $|E_{||}|$ with h_{bump} (see Fig. 12(c)). This explains why $|D_n|$ decreases with the bump height, since $|D_n| \approx |\varepsilon_0 b_n \varepsilon_{||} E_{||}|$ for the low plasma density considered here. Also, the similarity in the decrease rate with h_{bump} between $|V_{RF}|$ and $|D_n|$ (see Fig. 12(a) and (d)) is consistent with the relation $|V_{RF}| = \omega |D_n||z_{sh}|$ (see Eq. (3)) and $|z_{sh}|$ being nearly independent of the bump height (see Fig. 12(b)). The insensitivity of $|z_{sh}|$ to h_{bump} may be attributed to the cancelling effect of $|V_{RF}|$ and $|b_n|$ on $|z_{sh}|$; i.e., $|z_{sh}|$ (= $|y_{sh}|^{-1}$, where y_{sh} is the sheath admittance parameter) increases with the increase in $|V_{RF}|$ and the decrease in $|b_n|$ (see Fig. 6(a) and (b),

This manuscript was accepted by Phys. Plasmas. Click here to see the version of record.

respectively), and note that both $|V_{RF}|$ and $|b_n|$ decrease with the increase in the bump height. Thus, the dependences shown in Fig. 12 may be understood, at least in hindsight, from fundamental considerations; however, the complexities of the interaction emphasize the need for numerical calculations which implement the generalized sheath BC.

B. Higher density case

Second, we consider a higher density case where $n_0 = 2.4\times10^{17}$ m^{-3}, $B_{0x} = 4$ T, $B_{0y} = 0$ T, and $B_{0z} = 0.1$ T in the entire slab domain. This plasma density is slightly lower than the LHR density n_{LH} for the given parameters (i.e., $n_{LH} = 2.49\times10^{17}$ m^{-3}); thus, the SW still propagates in a similar way to that in Sec. IV A (see Fig. 11). Here, the interactions between SWs (with different electric field strengths) and sheaths are analyzed for $h_{bump} = 0$ and 0.4 m with K_{max} varied in the range of 400 to 1000 A/m in each case.

Figure 13(a) and (b) compare the profiles of $|V_{RF}|$ as a function of y on the sheath surface for $h_{bump} = 0$ and 0.4 m at $K_{max} = 600$ A/m, respectively; the results for $n_0 = 1\times10^{17}$ and 2.4×10^{17} m^{-3} are compared in each plot. It is seen in Fig. 13(b) that the bump introduces a noticeable asymmetry effect into the profile of $|V_{RF}|$ for $n_0 = 2.4\times10^{17}$ m^{-3}. Since the higher density case is near the lower hybrid resonance where $\varepsilon_\perp$ is close to zero by definition, the quantity $D_n \approx i\varepsilon_0\varepsilon_\times \mathbf{s}\cdot(\mathbf{b}\times\mathbf{E}) + \varepsilon_0 b_n \varepsilon_{||} E_{||}$ can be influenced by the

This manuscript was accepted by Phys. Plasmas. Click here to see the version of record.

electromagnetic $\varepsilon_\times$ term especially when $|b_n|$ is small (which reduces the $\varepsilon_\parallel$ term); a critical value of $|b_n|$ for which the two contributions to D_n become comparable is then given by $|b_n| = (\varepsilon_\times/\varepsilon_\parallel)|\mathbf{s}\cdot(\mathbf{b}\times\mathbf{E})/E_\parallel|$. Additional simulations (not illustrated) show that the asymmetry is lost if $\varepsilon_\times$ is artificially set to zero. The reason that the magnitude relation of $|V_{RF}|$ between the two density cases is reversed when the bump is formed on the sheath surface may be associated with the fact that $|\varepsilon_0 b_n \varepsilon_\parallel E_\parallel|$ in $|D_n|$ (see above) on the surface decreases more sensitively for $n_0 = 2.4\times10^{17}$ m^{-3} with the increase in the bump height.

Figure 14 shows the spatial variations of $|V_{RF}|$ and $|z_{sh}|$ as functions of y on the sheath surface at four different values of K_{max} for h_{bump} = 0 and 0.4 m with n_0 fixed at 2.4×10^{17} m^{-3}. We see that the profiles of $|V_{RF}|$ correspond to the profiles of $|z_{sh}|$; see Fig. 14(a) and (c) for the flat wall and Fig. 14(b) and (d) for the bump. The important point is that the asymmetry is amplified by the nonlinear response of the sheath impedance parameter with the $\varepsilon_\times$ term in D_n being dominant for h_{bump} = 0.4 m; as $|V_{RF}|$ increases more rapidly on one side of the bump with the increase in K_{max}, the rate of increase in $|z_{sh}|$ on that side becomes also greater than that on the other side of the bump, which further drives up $|V_{RF}|$ there. In fact, the asymmetry of the variations is a key factor that enables the maximum value of $|V_{RF}|$ for the bump to eventually exceed the one for the flat wall at the same value of K_{max} (in this analysis, at K_{max} = 1000 A/m). A qualitatively similar result was obtained in our

previous work; see Fig. 8 of Ref. 41.

V. CONCLUSIONS

In this paper, by using the new rfSOL code based on the sheath impedance model,[19,25,26] we have presented various properties which occur in association with the self-consistent RF sheath–plasma interactions for oblique-angle magnetic fields in low and high plasma densities (compared with the LHR density) at a wave frequency for ICRF heating. In some numerical examples, basically the same calculation conditions as the ones used in our previous paper[12] were chosen in order to compare the results obtained under the capacitive sheath BC (i.e., the previously used sheath BC) and the generalized sheath BC (i.e., the sheath BC corresponding to the sheath impedance model). It is expected that the generalized sheath BC should yield results closer to real phenomena, since it takes into account the total current density in the sheath (including the ion and electron current densities as well as the displacement current density), while only the displacement current contribution is considered in the capacitive sheath BC. The important findings of this study are summarized as follows.

In Sec. III, we solved the nonlinear sheath–plasma interaction problems in 2D slab geometry with a flat sheath surface. We first considered densities above the LHR density so

that the SW in the main plasma volume is evanescent. Under these conditions, it was demonstrated that the SPW, which propagates along the sheath surface and is evanescent into the plasma, disappears under the generalized sheath BC (in contrast with the corresponding result obtained under the capacitive sheath BC) for the chosen parameters. These parameters, in particular, included a small amount of antenna current density (implying a small RF sheath voltage), and the reason for the disappearance of the SPW was traced to the resistivity mainly caused by the electron current in the sheath. However, it was also shown that the SPW can still emerge even under the generalized sheath BC when the magnetic field line angle is small, the absolute value of the RF sheath voltage is large, and the plasma density is relatively low but still higher than the LHR density, with $\hat{\Omega}_i/\hat{\omega} = \Omega_i/\omega$ held constant. These conditions reduce the sheath resistance relative to the sheath capacitance. When the SPW is present, as in Fig. 4(b), it can be shown that some additional power, relative to the case without the SPW, flows along the sheath surface before being damped.

On the other hand, when considering the case where a propagating SW interacts with a sheath at a plasma density below the LHR density, no clear difference was seen in the numerical results obtained under the capacitive and generalized sheath BCs. The reason is that the imaginary part of the sheath impedance parameter is much greater than its real part in the region where the RF sheath is formed, which indicates that the capacitive sheath

approximation is valid for the given parameters. For this low density case, the maximum dissipated power per unit area on the sheath surface (i.e., the surface power density) is not so high (~ 100 kW/m^2), in contrast with the corresponding absolute value of the RF sheath voltage (~ 1 kV).

To investigate the effect of the magnetic field line angle on the nonlinear interactions, we employed a Gaussian-shaped bump on the sheath–plasma boundary of the 2D slab domain in Sec. IV. For the plasma density sufficiently lower than the LHR density, the effect of the magnetic field line angle was relatively weak within the range of the bump height considered in this analysis. Then, the absolute value of the RF sheath voltage, $|V_{\mathrm{RF}}|$, is determined mostly through the explicit dependence of $D_{\mathrm{n}} \approx \varepsilon_0 b_{\mathrm{n}} \varepsilon_{\parallel} E_{\parallel}$, since the absolute value of the sheath impedance parameter, $|z_{\mathrm{sh}}|$, is nearly independent of the bump height. On the other hand, for the plasma density slightly lower than the LHR density, it was demonstrated that the behavior of $|V_{\mathrm{RF}}|$ can become quite sensitive to the variation of the magnetic field line angle. In addition, the asymmetry and the sharp angle variation are responsible for the strong increase in $|V_{\mathrm{RF}}|$, which is further accentuated by the nonlinear increase in $|z_{\mathrm{sh}}|$.

In Ref. 12, multiple solutions of the nonlinear model using the capacitive sheath BC were found in one-dimensional simulations, associated with the presence of the SPW resonance. It is worth noting that we have not found any evidence for multiple solutions in the

2D simulations presented here, but also cannot claim with certainty that the solutions are unique. The dissipation in the generalized sheath BC model is one factor which can suppress sharp resonances and would likely also suppress multiple roots, since these depend sensitively on the structure of the SPW resonance.

In the present paper, we have only considered the interaction of RF waves with the sheaths they create on the RF time scale. Depending in part upon the properties of the external DC circuit connecting two ends of a given field line, and the asymmetry of the end sheaths, DC current can be driven by the rectified DC sheath potentials and flow along the field lines. In the present paper, we only consider the RF part of the problem, not the DC part or any coupling between the RF and DC circuits. DC currents have been observed in experiments in Refs. 44, 45 and incorporating them into simulations which couple the sheath current and voltage rectification effects in global tokamak geometry remains an important task for the RF modeling community.

Taken as a whole, this paper establishes the first numerical implementation of the generalized sheath BC for oblique-angle sheaths that we are aware of. We have shown that the generalized sheath BC produces results which appear to be physically plausible, and explained the reasons for similarities and differences with the purely capacitive sheath BC. Where possible, we have qualitatively explained the complicated variations of the sheath

voltage and other quantities on the sheath surface under the generalized sheath BC. We hope that the present work is useful in understanding the behavior of the generalized sheath BC under a variety of conditions. It is also hoped that the sample cases investigated in this study may prove useful as verification test cases for benchmarking other codes which implement the generalized sheath BC.

Further development of the rfSOL code will be required to apply it to the problems including electron-rich sheaths (where the values of $|b_n|$ are very small). The reassessment of the present form of the sheath BC will also be required for cases where sharp corners are present on the boundary of the calculation domain and sheaths are formed there. Finally, specific implications for antenna design and tokamak operation remain the subject of future work.

ACKNOWLEDGMENTS

This material is based upon work supported by JSPS KAKENHI Grant Number JP16K18336 and the U.S. Department of Energy Office of Science, Office of Fusion Energy Sciences, under Award Nos. DE-FG02-97ER54392 and DE-AC05-00OR22725 (subcontract 4000158507). This research used resources of the National Energy Research Scientific

Computing Center, a DOE Office of Science User Facility supported by the Office of Science of the U.S. Department of Energy under Contract No. DE-AC02-05CH11231.

APPENDIX A: SHEATH ADMITTANCE PARAMETER FOR PERPENDICULAR SHEATHS

In this appendix, we demonstrate that the recently proposed functional forms used to compute the (total) dimensionless sheath admittance parameter $\hat{y}_{sh}$ (see Ref. 26) yield values similar to the ones computed using the previous functions[19] for perpendicular sheaths. Figure 15(a) and (b) show the filled contour plots of $\mathrm{Re}(\hat{y}_{sh})$, which are obtained by employing the previous and new expressions for the dimensionless admittance parameter, respectively, over the validity range of the previous expressions, i.e., $0 < \hat{\omega} < 8$ and $0 < \tilde{V}_{pp} < 20$, where $\tilde{V}_{pp}$ is the dimensionless peak-to-peak voltage expressed by $\tilde{V}_{pp} = 2\tilde{V}_{RF}$. It is seen that the profiles are very similar to each other, which indicates that all the results shown in Ref. 19 should be reproduced even with the use of $\hat{y}_{sh}$ (or $\hat{z}_{sh}$) in Ref. 26. However, note that the most recent formulation of the sheath admittance parameter removes the necessity to set upper limits of $\hat{\omega}$ and $\tilde{V}_{pp}$ for the perpendicular sheath case and is also valid for oblique angles.

This manuscript was accepted by Phys. Plasmas. Click here to see the version of record.

Figure Captions

FIG. 1. Singly periodic slab model with a flat sheath surface.

FIG. 2. (Color online) Filled contour plots of $\mathrm{Re}\left(E_{\|}\right)$ for $n_0 = 2\times10^{18}$ m^{-3}, $B_{0x} = 1.5$ T, $B_{0y} = 0.5$ T, $B_{0z} = 4$ T, and $K_{\max} = 1$ A/m under the capacitive sheath BC (a) and the generalized sheath BC (b). The nonlinear numerical scheme is employed to obtain the result in (a), although the nonlinear contribution in the capacitive sheath BC is negligibly small in this case. [Associated dataset available at http://doi.org/10.5281/zenodo.1667247] (Ref. 40).

FIG. 3. (Color online) Plots of the real and imaginary parts of k_y at the sheath surface as functions of the plasma density, which are obtained by employing the capacitive sheath BC (a) and the generalized sheath BC (b) without including the RF contribution. The plot shown in (a) is obtained by replacing $\hat{y}_{\mathrm{sh}}$ with $\hat{y}_{\mathrm{d}}$ in the code into which Eqs. (9) and (10) are incorporated; note that this plot is almost identical with the plot shown in Fig. 4 of Ref. 12, which assures the validity of the present code based on the generalized sheath BC (given in Eq. (9)). The fixed parameters are $B_{0x} = 1.5$ T, $B_{0y} = 0.5$ T, $B_{0z} = 4$ T, $T_{\mathrm{e}} = 10$ eV, $k_z = 10.8$ m^{-1}, $f = 80$ MHz, and $\tilde{V}_{\mathrm{RF}} = 0$. The gray vertical line in (a) and (b) indicates the

density value used in the numerical simulation. [Associated dataset available at http://doi.org/10.5281/zenodo.1667247] (Ref. 40).

FIG. 4. (Color online) Filled contour plots of $\mathrm{Re}\left(E_{\parallel}\right)/K_{\max}$ for $n_0 = 6\times10^{17}$ m^{-3}, B_{0x} = 0.5 T, B_{0y} = 1.5 T, and B_{0z} = 4 T at $K_{\max}$ = 1 A/m (a) and $K_{\max}$ = 100 A/m (b), which are obtained under the generalized sheath BC. [Associated dataset available at http://doi.org/10.5281/zenodo.1667247] (Ref. 40).

FIG. 5. (Color online) Plot of the real and imaginary parts of k_y at the sheath surface as functions of the normalized RF sheath voltage $\tilde{V}_{\mathrm{RF}}$, which is obtained based on the sheath impedance model. The fixed parameters are B_{0x} = 0.5 T, B_{0y} = 1.5 T, B_{0z} = 4 T, n_0 = 6×10^{17} m^{-3}, T_{e} = 10 eV, k_z = 10.8 m^{-1}, and f = 80 MHz. The gray vertical line indicates $\tilde{V}_{\mathrm{RF}}$ = 28.4, which corresponds to the maximum absolute value of the RF sheath voltage on the sheath surface in the numerical solution for $K_{\max}$ = 100 A/m (see Fig. 4(b)). [Associated dataset available at http://doi.org/10.5281/zenodo.1667247] (Ref. 40).

FIG. 6. (Color online) Plots of the dimensionless sheath admittance parameter $\hat{y}_{\mathrm{sh}}$ and the dimensionless displacement admittance parameter $\hat{y}_{\mathrm{d}}$ vs. $\tilde{V}_{\mathrm{RF}}$ (a), $|b_{\mathrm{n}}|$ (b), and n_0 (c).

This manuscript was accepted by Phys. Plasmas. Click here to see the version of record.

Here, $\mathrm{Re}(\hat{y}_{\mathrm{sh}})$, $\mathrm{Im}(\hat{y}_{\mathrm{sh}})$, and $\mathrm{Im}(\hat{y}_{\mathrm{d}})$ are denoted by black solid curves, black dashed curves, and red dashed curves, respectively. The fixed parameters are as follows: B_{0x} = 0.5 T, B_{0y} = 1.5 T, B_{0z} = 4 T, n_0 = 6×10^{17} m^{-3}, and f = 80 MHz in (a); $|\mathbf{B}_0|$ = 4.3 T, n_0 = 6×10^{17} m^{-3}, f = 80 MHz, and $\tilde{V}_{\mathrm{RF}}$ = 28.4 in (b); and B_{0x} = 0.5 T, B_{0y} = 1.5 T, B_{0z} = 4 T, f = 80 MHz, and $\tilde{V}_{\mathrm{RF}}$ = 28.4 in (c). The gray vertical line in each plot indicates the value (on the horizontal axis) that yields $\mathrm{Re}(\hat{y}_{\mathrm{sh}})$ = 9.62×10^{-3} and $\mathrm{Im}(\hat{y}_{\mathrm{sh}})$ = -3.46×10^{-2}, i.e., the minimum value of $|\hat{y}_{\mathrm{sh}}|$ on the sheath surface in the numerical solution for $K_{\max}$ = 100 A/m. [Associated dataset available at http://doi.org/10.5281/zenodo.1667247] (Ref. 40).

FIG. 7. (Color online) Filled contour plots of $\mathrm{Re}(E_{\parallel})/K_{\max}$ for n_0 = 1×10^{17} m^{-3}, B_{0x} = 1.5 T, B_{0y} = 0.5 T, and B_{0z} = 4 T at $K_{\max}$ = 160 A/m under the capacitive sheath BC (a) and the generalized sheath BC (b). [Associated dataset available at http://doi.org/10.5281/zenodo.1667247] (Ref. 40).

FIG. 8. Plot of the real and imaginary parts of z_{sh} along the sheath surface at $K_{\max}$ = 160 A/m, which is obtained by employing the generalized sheath BC. [Associated dataset available at http://doi.org/10.5281/zenodo.1667247] (Ref. 40).

FIG. 9. (Color online) Plots of $|V_{RF}|$ (a), V_{rect} (b), and P_{yz} (c) along the sheath surface at four different values of K_{max}, which are obtained by employing the generalized sheath BC. [Associated dataset available at http://doi.org/10.5281/zenodo.1667247] (Ref. 40).

FIG. 10. Singly periodic slab model with a bump in the sheath surface.

FIG. 11. (Color online) Filled contour plot of $\mathrm{Re}(E_{\|})/K_{max}$ for $n_0 = 1\times10^{17}$ m^{-3}, $B_{0x} = 4$ T, $B_{0y} = 0$ T, $B_{0z} = 0$ T, and $K_{max} = 600$ A/m at $h_{bump} = 0.4$ m, which is obtained under the generalized sheath BC. [Associated dataset available at http://doi.org/10.5281/zenodo.1667247] (Ref. 40).

FIG. 12. (Color online) Plots of $|V_{RF}|$ (a), $|z_{sh}|$ (b), $|E_{\|}|$ (c), and $|D_n|$ (d) as functions of y on the sheath surface at four different values of h_{bump} for $n_0 = 1\times10^{17}$ m^{-3} with K_{max} fixed at 600 A/m. [Associated dataset available at http://doi.org/10.5281/zenodo.1667247] (Ref. 40).

FIG. 13. Comparison of the plots of $|V_{RF}|$ as a function of y at $K_{max} = 600$ A/m and two different values of n_0 for $h_{bump} = 0$ m (a) and $h_{bump} = 0.4$ m (b). [Associated dataset

available at http://doi.org/10.5281/zenodo.1667247] (Ref. 40).

FIG. 14. (Color online) Plots of $|V_{RF}|$ vs. y for h_{bump} = 0 m (a) and h_{bump} = 0.4 m (b) and plots of $|z_{sh}|$ vs. y for h_{bump} = 0 m (c) and h_{bump} = 0.4 m (d) on the sheath surface at four different values of K_{max}. Here, the plasma density n_0 is fixed at 2.4×10^{17} m^{-3}. [Associated dataset available at http://doi.org/10.5281/zenodo.1667247] (Ref. 40).

FIG. 15. (Color online) Comparison of the filled contour plots of $\mathrm{Re}(\hat{y}_{sh})$ as a function of $\hat{\omega}$ and $\tilde{V}_{pp}$ for perpendicular sheaths, which are obtained using the functions presented in Ref. 19 (a) and the functions presented in Ref. 26 (b). [Associated dataset available at http://doi.org/10.5281/zenodo.1667247] (Ref. 40).

Please note: The widths of the figures should be adjusted to coincide with two-column width (i.e., a width of the paper) or one-column width (i.e., a half width of the paper). Also, please trim away unnecessary parts of the figures.

References

[1] T. H. Stix, *Waves in Plasmas* (American Institute of Physics, 1992).
[2] J.-M. Noterdaeme and G. Van Oost, Plasma Phys. Controlled Fusion 35, 1481 (1993).
[3] J. R. Myra, D. A. D'Ippolito, D. A. Russell, L. A. Berry, E. F. Jaeger, and M. D. Carter, Nucl. Fusion **46**, S455 (2006).
[4] F. W. Perkins, Nucl. Fusion **29**, 583 (1989).
[5] D. A. D'Ippolito, J. R. Myra, J. Jacquinot, and M. Bures, Phys. Fluids B **5**, 3603 (1993).
[6] M. Bécoulet, L. Colas, S. Pécoul, J. Gunn, Ph. Ghendrih, A. Bécoulet, and S. Heuraux, Phys. Plasmas **9**, 2619 (2002).
[7] L. Colas, S. Heuraux, S. Brémond, and G. Bosia, Nucl. Fusion **45**, 767 (2005).
[8] V. Bobkov, F. Braun, R. Dux, A. Herrmann, H. Faugel, H. Fünfgelder, A. Kallenbach, R. Neu, J.-M. Noterdaeme, R. Ochoukov, Th. Pütterich, A. Tuccillo, O. Tudisco, Y. Wang, Q. Yang, and ASDEX Upgrade team, Nucl. Fusion **56**, 084001 (2016).
[9] S. J. Wukitch, M. L. Garrett, R. Ochoukov, J. L. Terry, A. Hubbard, B. Labombard, C. Lau, Y. Lin, B. Lipschultz, D. Miller, M. L. Reinke, D. Whyte, and Alcator C-Mod Team, Phys. Plasmas **20**, 056117 (2013).
[10] F. Waelbroeck, J. Winter, G. Esser, B. Giesen, L. Könen, V. Philipps, U. Samm, J. Schlüter, P. Weinhold, the TEXTOR Team, and T. Banno, Plasma Phys. Controlled Fusion **31**, 185 (1989).
[11] J. R. Myra and D. A. D'Ippolito, Plasma Phys. Controlled Fusion **52**, 015003 (2010).
[12] H. Kohno, J. R. Myra, and D. A. D'Ippolito, Phys. Plasmas **19**, 012508 (2012).
[13] D. Van Eester, K. Crombé, and V. Kyrytsya, Plasma Phys. Controlled Fusion **55**, 055001 (2013).
[14] D. A. D'Ippolito, J. R. Myra, R. Ochoukov, and D. G. Whyte, Plasma Phys. Controlled Fusion **55**, 085001 (2013).
[15] H. Kohno, J. R. Myra, and D. A. D'Ippolito, Phys. Plasmas **20**, 082514 (2013).
[16] N. Bertelli, E. F. Jaeger, J. C. Hosea, C. K. Phillips, L. Berry, S. P. Gerhardt, D. Green, B. LeBlanc, R. J. Perkins, P. M. Ryan, G. Taylor, E. J. Valeo, and J. R. Wilson, Nucl. Fusion **54**, 083004 (2014).
[17] D. N. Smithe, D. A. D'Ippolito, and J. R. Myra, AIP Conf. Proc. **1580**, 89 (2014).
[18] L. Colas, L.-F. Lu, A. Křivská, J. Jacquot, J. Hillairet, W. Helou, M. Goniche, S. Heuraux, and E. Faudot, Plasma Phys. Controlled Fusion **59**, 025014 (2017).
[19] H. Kohno and J. R. Myra, Comput. Phys. Commun. **220**, 129 (2017).
[20] M. A. Lieberman, IEEE Trans. Plasma Sci. **16**, 638 (1988).
[21] J. R. Myra, D. A. D'Ippolito, and M. Bures, Phys. Plasmas **1**, 2890 (1994).
[22] E. F. Jaeger, L. A. Berry, J. S. Tolliver, and D. B. Batchelor, Phys. Plasmas **2**, 2597 (1995).
[23] D. A. D'Ippolito and J. R. Myra, Phys. Plasmas **13**, 102508 (2006).
[24] T. G. Jenkins and D. N. Smithe, Plasma Sources Sci. Technol. **24**, 015020 (2015).
[25] J. R. Myra and D. A. D'Ippolito, Phys. Plasmas **22**, 062507 (2015).
[26] J. R. Myra, Phys. Plasmas **24**, 072507 (2017).
[27] M. J. Martin, W. Gekelman, B. Van Compernolle, P. Pribyl, and T. Carter, Phys. Rev. Lett. **119**, 205002 (2017).
[28] K. Crombé, S. Devaux, R. D'Inca, E. Faudot, H. Faugel, H. Fünfgelder, S. Heuraux, J. Jacquot, F. Louche, J. Moritz, R. Ochoukov, M. Tripsky, D. Van Eester, T. Wauters, and J.-M.

Noterdaeme, AIP Conf. Proc. **1689**, 030006 (2015).
[29] P. A. Piotrowicz, J. F. Caneses, D. L. Green, R. H. Goulding, C. Lau, J. B. O. Caughman, J. Rapp, and D. N. Ruzic, Plasma Sources Sci. Technol. **27**, 055016 (2018).
[30] E. Faudot, S. Devaux, J. Moritz, V. Bobkov, and S. Heuraux, EPJ Web of Conferences **157**, 03013 (2017).
[31] L. Colas, J. Jacquot, S. Heuraux, E. Faudot, K. Crombé, V. Kyrytsya, J. Hillairet, and M. Goniche, Phys. Plasmas **19**, 092505 (2012).
[32] W. Tierens, J. Jacquot, V. Bobkov, J. M. Noterdaeme, L. Colas, and The ASDEX Upgrade Team, Nucl. Fusion **57**, 116034 (2017).
[33] J. Jacquot, D. Milanesio, L. Colas, Y. Corre, M. Goniche, J. Gunn, S. Heuraux, and M. Kubič, Phys. Plasmas **21**, 061509 (2014).
[34] L. Lu, L. Colas, J. Jacquot, B. Després, S. Heuraux, E. Faudot, D. Van Eester, K. Crombé, A. Křivská, J-M. Noterdaeme, W. Helou, and J. Hillairet, Plasma Phys. Controlled Fusion **60**, 035003 (2018).
[35] W. Zhang, W. Tierens, J-M. Noterdaeme, V. Bobkov, D. Aguiam, D. Coster, H. Fuenfgelder, J. Jacquot, R. Ochoukov, A. Silva, L. Colas, A. Křivská, the ASDEX Upgrade team, and the MST1 team, Nucl. Fusion **57**, 116048 (2017).
[36] H. Kohno, J. R. Myra, and D. A. D'Ippolito, Comput. Phys. Commun. **183**, 2116 (2012).
[37] J. R. Myra and H. Kohno, EPJ Web of Conferences **157**, 03037 (2017).
[38] L. Colas, V. Basiuk, B. Beaumont, A. Bécoulet, G. Bosia, S. Brémond, M. Chantant, F. Clairet, A. Ekedahl, E. Faudot, A. Géraud, M. Goniche, S. Heuraux, G. T. Hoang, G. Lombard, L. Millon, R. Mitteau, P. Mollard, K. Vulliez, and the Tore Supra team, Nucl. Fusion **46**, S500 (2006).
[39] P. Jacquet, L. Colas, M.-L. Mayoral, G. Arnoux, V. Bobkov, M. Brix, P. Coad, A. Czarnecka, D. Dodt, F. Durodie, A. Ekedahl, D. Frigione, M. Fursdon, E. Gauthier, M. Goniche, M. Graham, E. Joffrin, A. Korotkov, E. Lerche, J. Mailloux, I. Monakhov, C. Noble, J. Ongena, V. Petrzilka, C. Portafaix, F. Rimini, A. Sirinelli, V. Riccardo, Z. Vizvary, A. Widdowson, K.-D. Zastrow, and JET EFDA Contributors, Nucl. Fusion **51**, 103018 (2011).
[40] H. Kohno and J. R. Myra (2018). "Radio-frequency wave interactions with a plasma sheath in oblique-angle magnetic fields using a sheath impedance model," Zenodo. http://doi.org/10.5281/zenodo.1667247.
[41] H. Kohno, J. R. Myra, and D. A. D'Ippolito, Phys. Plasmas **22**, 072504 (2015); Ibid., Phys. Plasmas **23**, 089901 (2016).
[42] D. A. D'Ippolito and J. R. Myra, Phys. Plasmas **3**, 420 (1996).
[43] P. C. Stangeby, *The Plasma Boundary of Magnetic Fusion Devices*, *Plasma Physics Series* (Institute of Physics Publishing, 2000).
[44] R. Van Nieuwenhove and G. Van Oost, Plasma Phys. Controlled Fusion **34**, 525 (1992).
[45] R. J. Perkins, J. C. Hosea, M. A. Jaworski, R. E. Bell, N. Bertelli, G. J. Kramer, L. Roquemore, G. Taylor, and J. R. Wilson, Nucl. Mater. Energy **12**, 283 (2017).

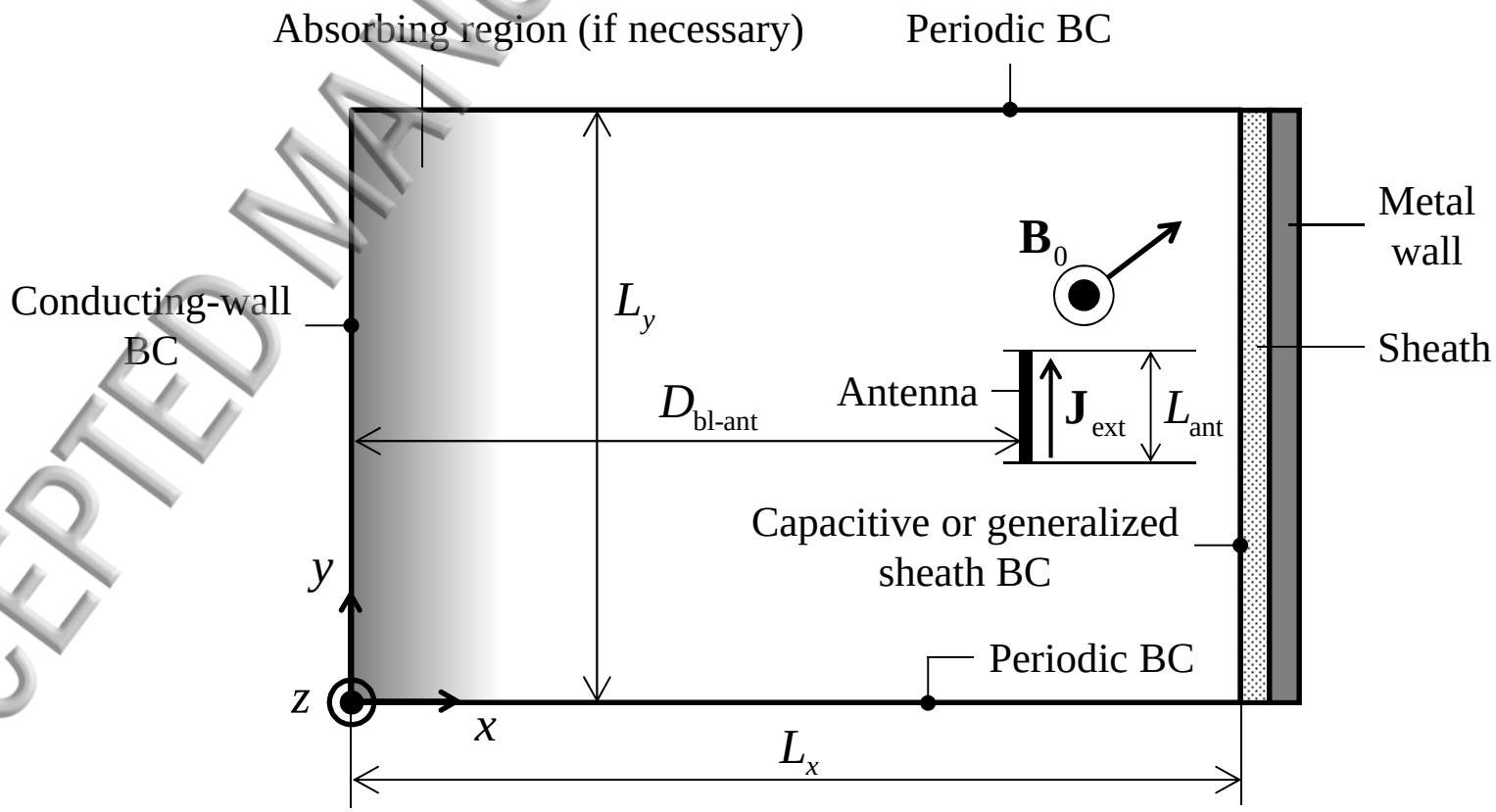

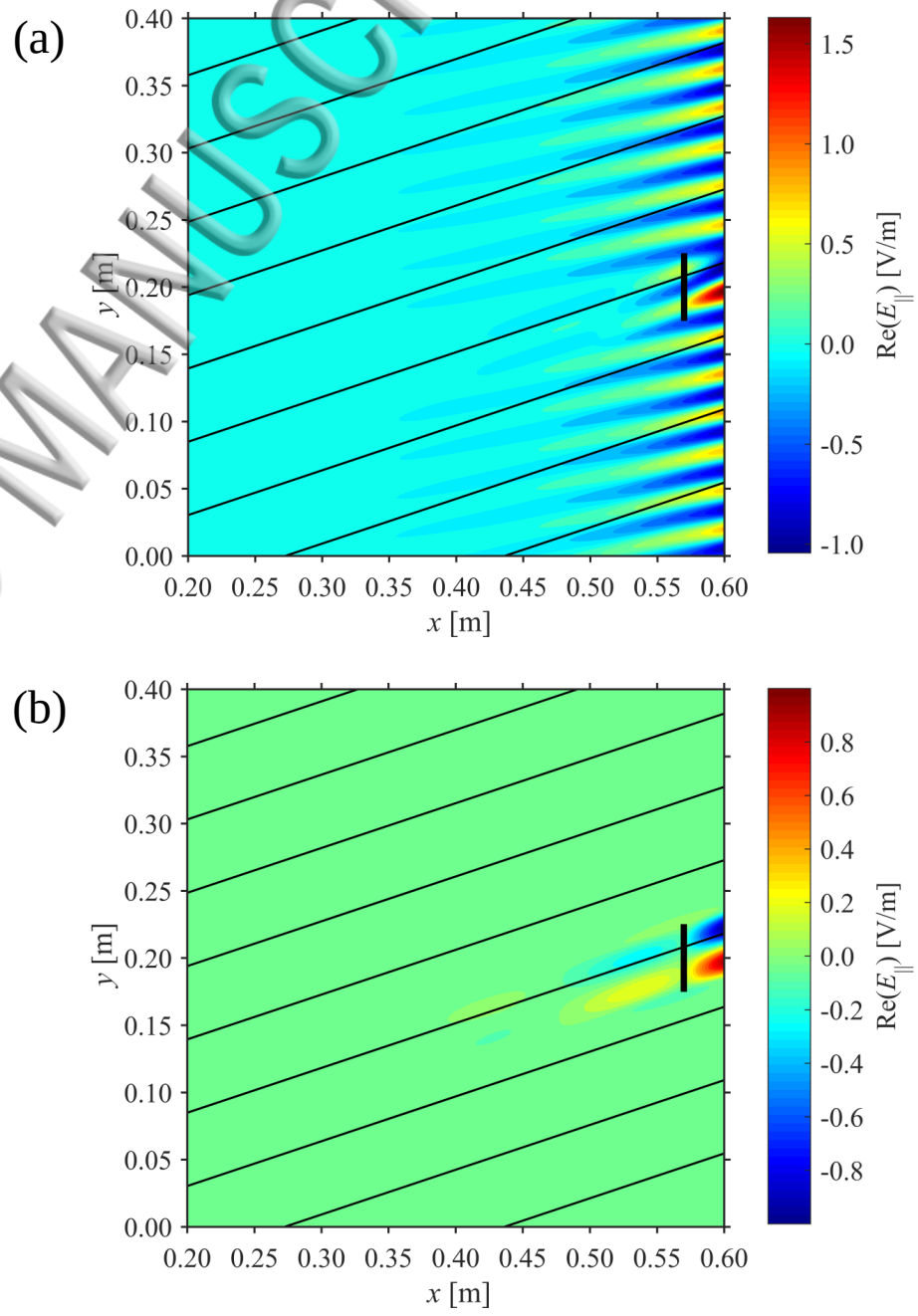

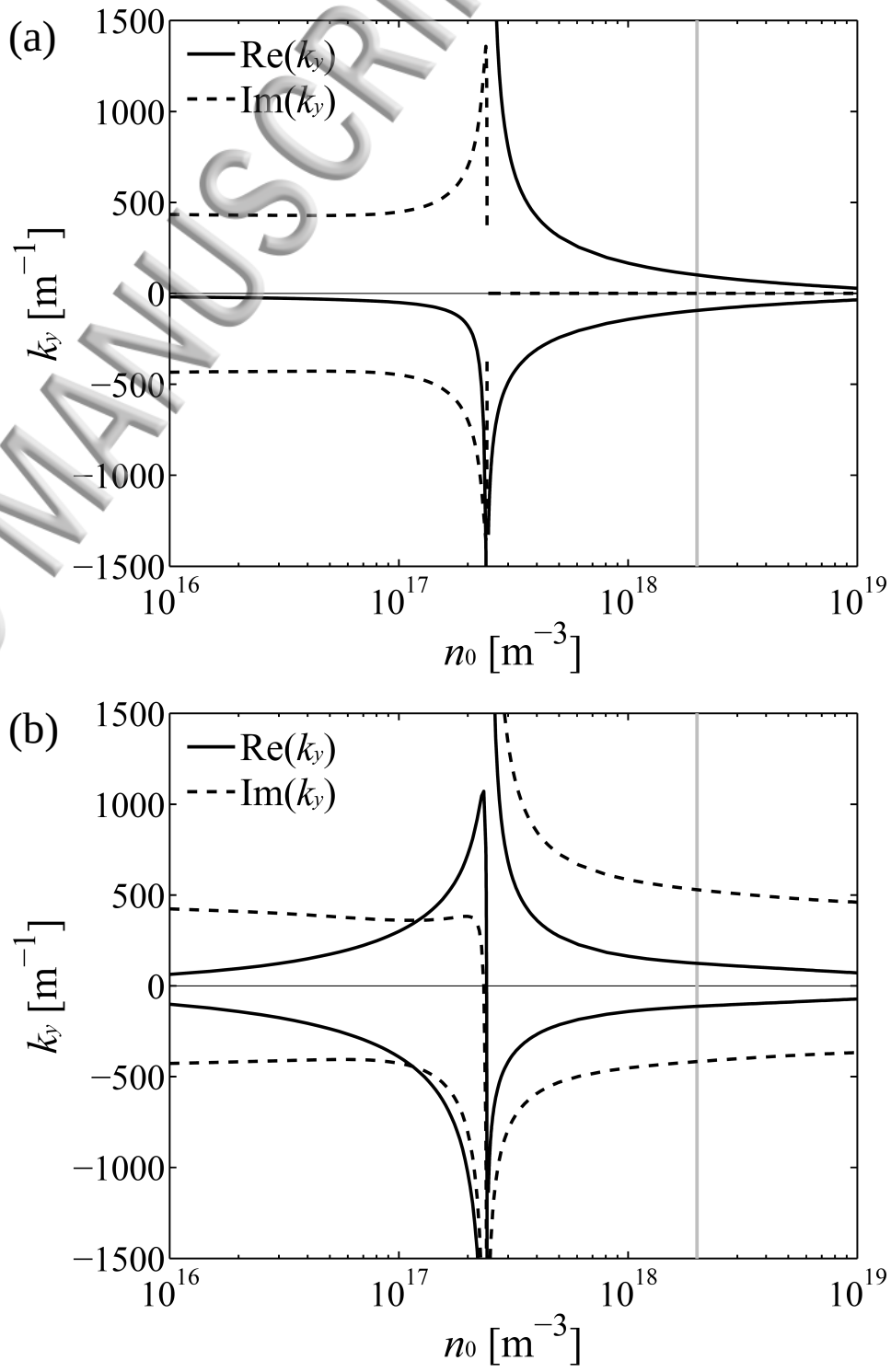

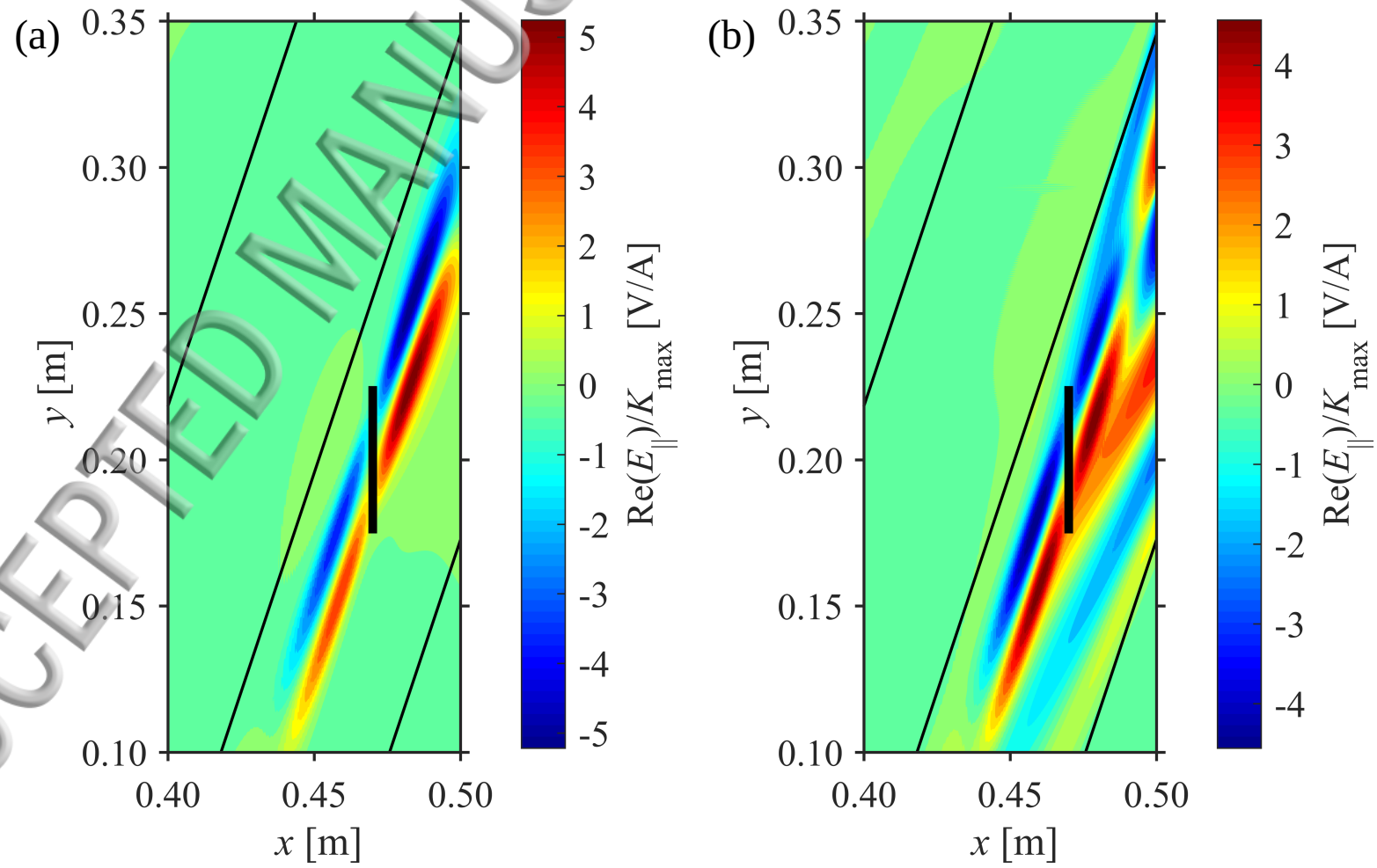

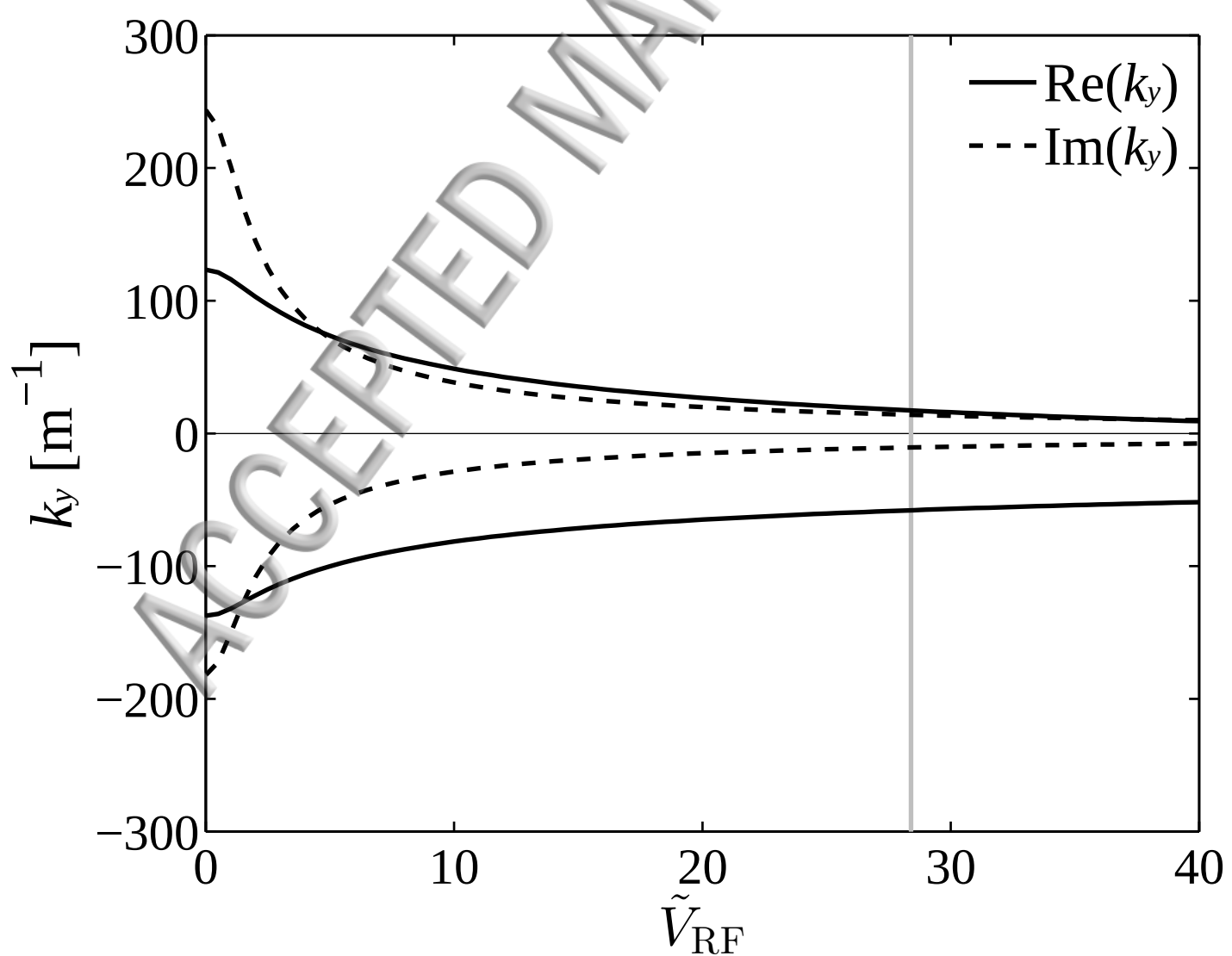
300
200
100
0
−100
−200
−300
0
10
20
30
40
k_y [m^{-1}]
$\tilde{V}_{\mathrm{RF}}$
Re(k_y)
Im(k_y)

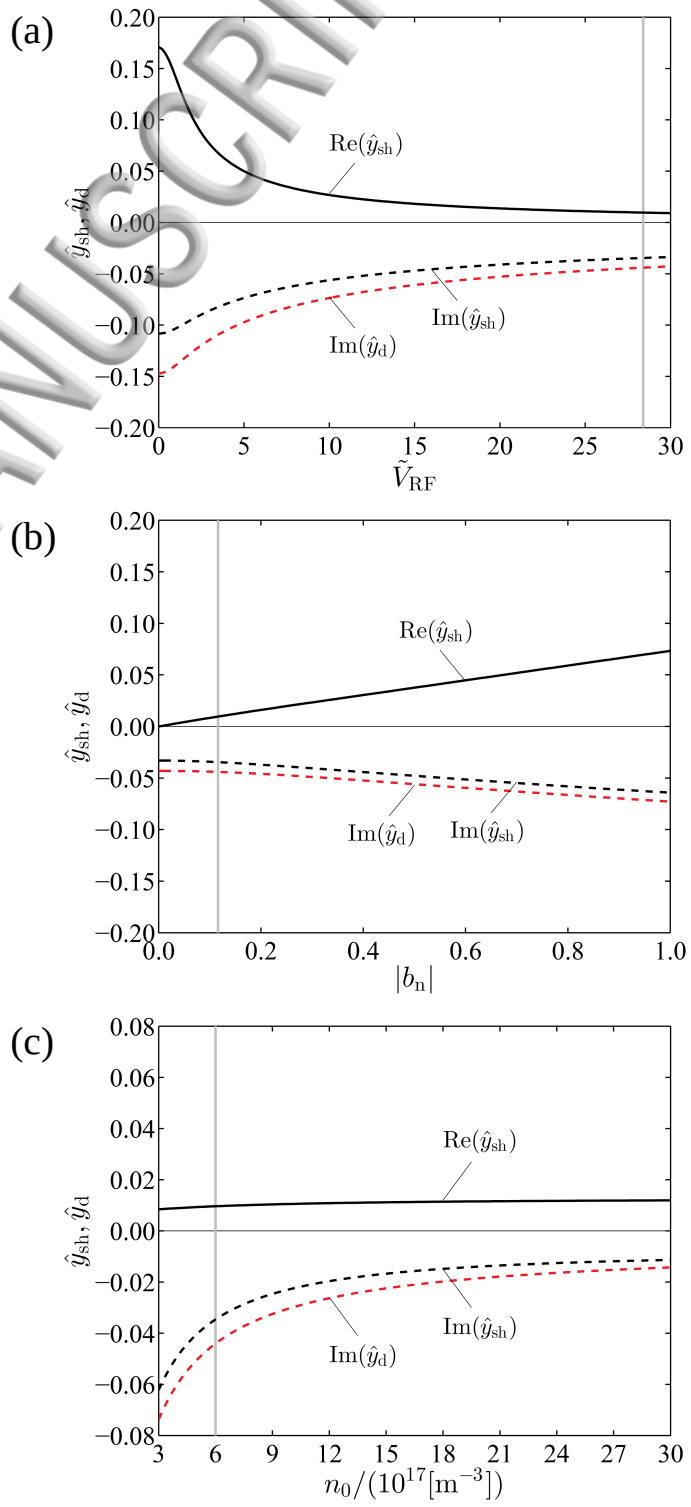

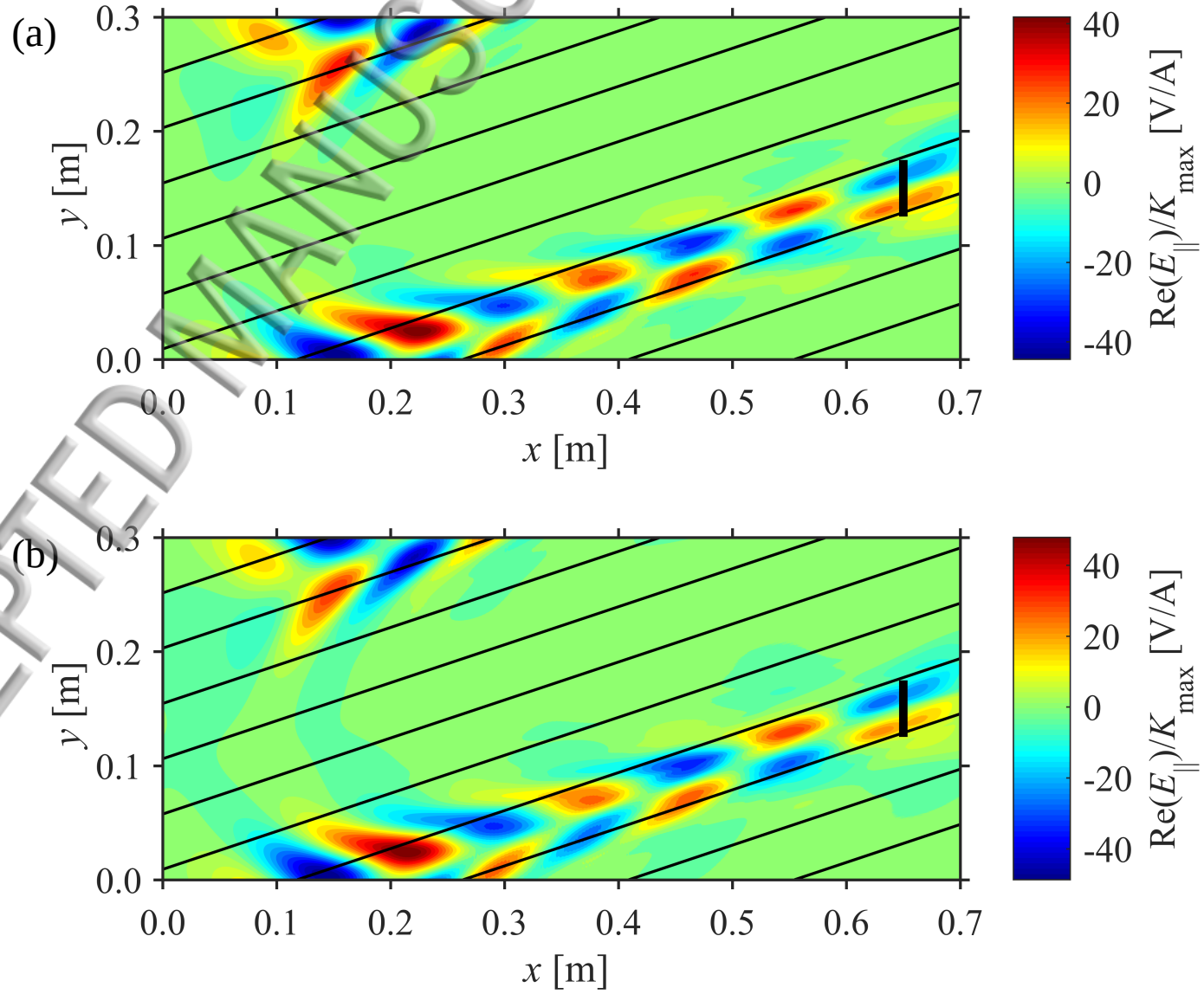

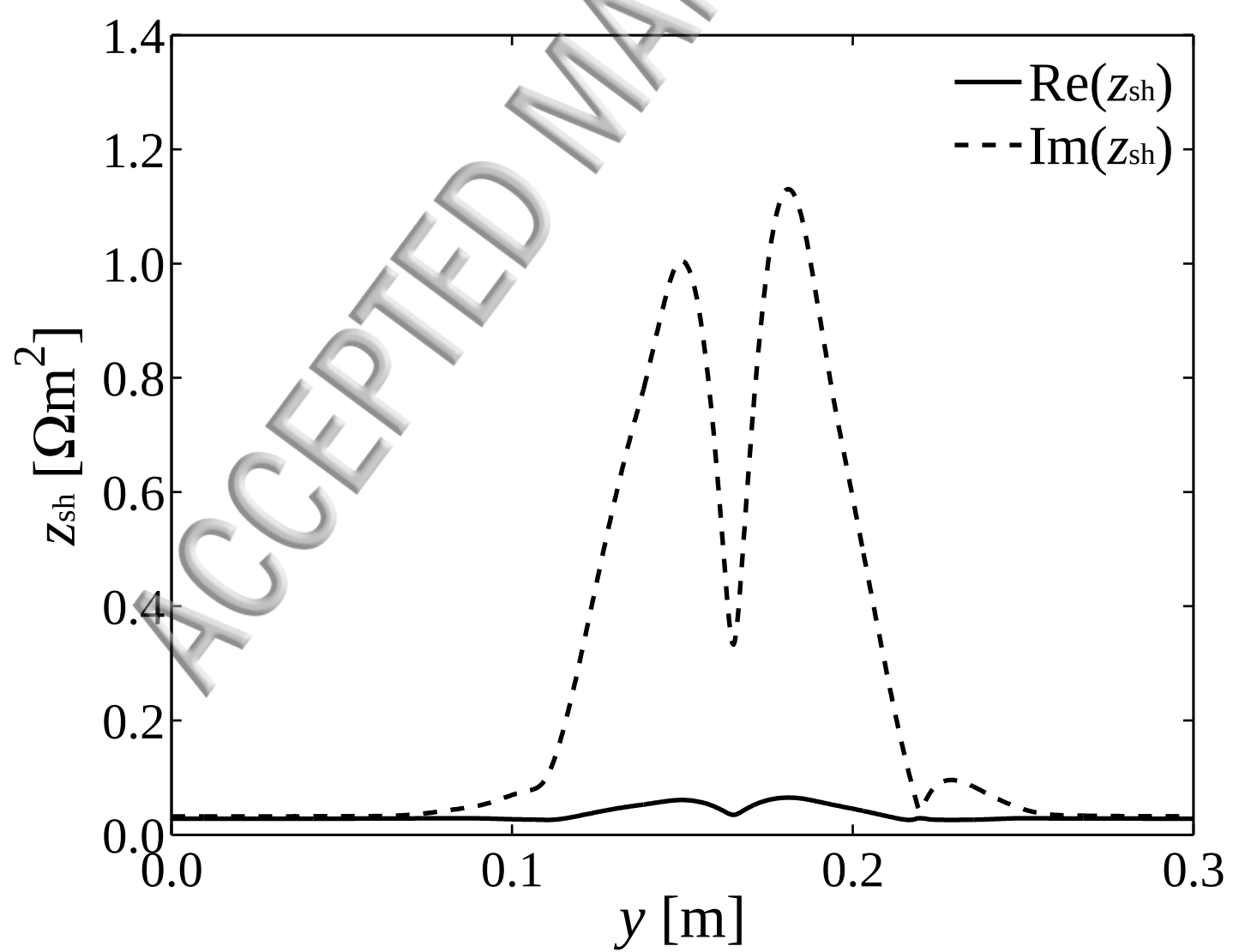

(a)

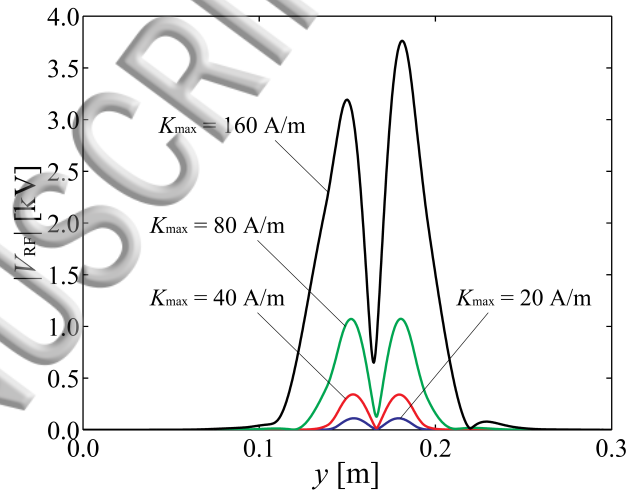

(b)

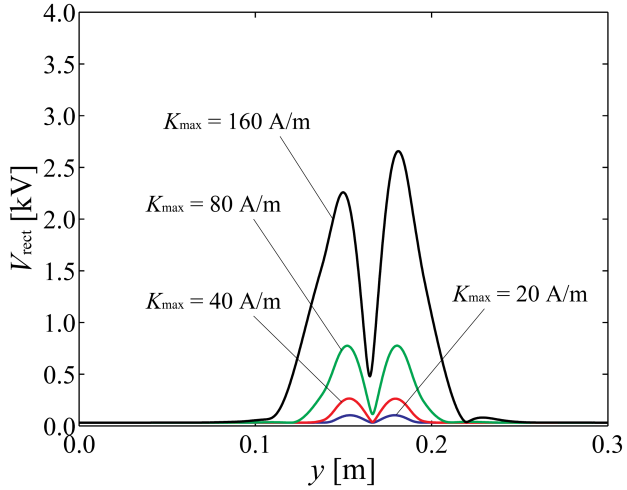

(c)